Simulation of dust aerosol radiative feedback using the GMOD: 2. Dust-climate interactions

Xu Yue,[1,2,3,4] Huijun Wang,[1,2] Hong Liao,[5,6] and Ke Fan[2]

[1] We examine equilibrium climate responses to the shortwave and/or longwave direct radiative effect of mineral dust aerosol using the Global transport Model of Dust (GMOD) embedded within a general circulation model (GCM). The presence of mineral dust aerosol in the atmosphere is estimated to exert global mean shortwave and longwave radiative forcings (RF) of -0.25 W m^{-2} and $+0.27$ W m^{-2}, respectively, at the top of the atmosphere (TOA) and -1.95 W m^{-2} and $+0.61$ W m^{-2} at the surface. Climatic effect of dust is simulated using two different approaches. In the first approach, monthly mean fields of dust simulated a priori are used in the radiative transfer module of the GCM to drive climate change, with levels of dust fixed during the climate integration (denoted as simulation FIXDST). In the second approach, dust aerosol interacts online with meteorology through the dust cycle and its direct radiative effect (denoted as simulation CPLD). With both longwave and shortwave RF of dust, predicted changes in global and annual mean surface air temperature and air temperature at 200 hPa are zero and $+0.12$ K, respectively, in FIXDST, and -0.06 K and $+0.05$ K in the CPLD simulation. The stronger cooling in CPLD than in FIXDST is a result of a 13% higher dust burden in CPLD with dust-climate interactions. Although dust longwave radiative effect is predicted to offset a large portion of its shortwave effect on a global and annual mean basis, dust shortwave effect dominates during the daytime, and the longwave effect prevails at night, which is found to be very important for predictions of temperature. For example, over the Sahara Desert, the changes in annual mean, annual mean daytime, and annual mean nighttime surface air temperature are predicted to be $+0.32$ K, -0.11 K, and $+0.68$ K, respectively, in the FIXDST simulation. The longwave and shortwave radiative effects of dust are predicted to have different impacts on the dust cycle in CPLD simulation; the solar radiative effect reduces dust emissions by increasing surface humidity and by reducing surface wind speed, while the thermal effect increases dust uplift through opposite changes in the meteorological parameters.

1. Introduction

[2] Mineral dust aerosol can influence climate directly by scattering and absorption of solar and/or longwave radiation [*Carlson and Benjamin*, 1980; *Sokolik and Toon*, 1996; *Miller and Tegen*, 1998] and indirectly by changing the optical properties and lifetime of clouds [*Sassen*, 2002; *Lohmann and Diehl*, 2006]. Radiative forcing (RF) of dust aerosol is sensitive to a number of key variables such as the imaginary part of the refractive index, particle size, vertical profile of dust, surface albedo, presence of clouds, and atmospheric temperature [*Tegen and Lacis*, 1996; *Claquin et al.*, 1998; *Liao and Seinfeld*, 1998; *Sokolik and Toon*, 1999; *Harrison et al.*, 2001; *Shi et al.*, 2005]. The lack of global constraints of these variables by observations leads to great uncertainties in simulations of climatic impacts of mineral dust aerosol.

[3] Mineral dust aerosol exerts RF in both shortwave and longwave spectral regions. The shortwave radiative effect, the scattering and absorption of solar radiation, has been found to reduce the downward shortwave radiation that reaches the Earth's surface, leading to a cooling at the surface and in the lower troposphere [*Miller and Tegen*, 1998; *Ahn et al.*, 2007; *Shell and Somerville*, 2007]. A cooling of $0.1–0.5$ K at the surface and the 850 hPa altitude was

---

[1]Climate Change Research Center, Chinese Academy of Sciences, Beijing, China.
[2]Nansen-Zhu International Research Center, Institute of Atmospheric Physics, Chinese Academy of Sciences, Beijing, China.
[3]Graduate School of the Chinese Academy of Sciences, Beijing, China.
[4]Now at School of Engineering and Applied Sciences, Harvard University, Cambridge, Massachusetts, USA.
[5]National Laboratory of Atmospheric Boundary Layer Physics and Atmospheric Chemistry, Institute of Atmospheric Physics, Chinese Academy of Sciences, Beijing, China.
[6]Also at Climate Change Research Center, Chinese Academy of Sciences, Beijing, China.

simulated in East Asia during an Asian dust event [*Ahn et al.*, 2007]. In the upper troposphere, the absorption of both incoming and reflected solar radiation by dust particles increases the air temperature [*Alpert et al.*, 1998; *Miller and Tegen*, 1998; *Satheesh et al.*, 2007]. In a case study, a heating rate of $\sim$0.2 K d^{-1} between 850 and 650 hPa was estimated over the eastern tropical North Atlantic Ocean [*Alpert et al.*, 1998].

[4] Measurements and models have shown that the absorption and emission of infrared radiation by mineral dust have a large impact on the longwave radiative balance. Dust particles increase the downward longwave radiation at the surface [*Cautenet et al.*, 1991; *Markowicz et al.*, 2003] while reducing outgoing longwave radiation at the top of the atmosphere (TOA) [*Ackerman and Chung*, 1992; *Haywood et al.*, 2005]. The longwave RF of dust at the surface was found to be larger than that at the TOA [*Markowicz et al.*, 2003], which can greatly offset the shortwave RF of dust found at the surface [*Lubin et al.*, 2002; *Zhang and Christopher*, 2003; *Christopher and Jones*, 2007]. *Ackerman and Chung* [1992] reported, by using model calculations and measurements from the Earth Radiation Budget Experiment (ERBE), that mineral dust aerosol led to reductions of TOA outgoing longwave radiation by 5–20 W m^{-2} over the oceans and by 20–50 W m^{-2} over the deserts during a dust outbreak that occurred over the Saudi Arabian peninsula in July 1985.

[5] The radiative effect of mineral dust aerosol leads to changes in meteorological parameters. The surface cooling by dust shortwave RF results in large reductions in latent and sensible heat fluxes from the surface to the atmosphere [*Miller et al.*, 2004b; *Shell and Somerville*, 2007], which, to some extent, helps to compensate the surface cooling and atmosphere warming. The changes in surface latent heat flux correlate with surface evaporation, causing a reduction in total precipitation [*Miller and Tegen*, 1998]. Furthermore, the reduction in sensible heat flux reduces the turbulent energy within the planetary boundary layer (PBL) and the downward transport of momentum to the surface, which has an effect of reducing surface wind speed [*Miller et al.*, 2004a]. Among previous studies that examined climate responses to dust RF, most simulations considered either the shortwave effect of dust alone [*Yoon et al.*, 2005; *Bar-Or et al.*, 2008] or the net effect of both shortwave and longwave dust forcing [*Miller and Tegen*, 1998; *Heinold et al.*, 2007]. Few studies have quantified the climatic impact of dust longwave radiative effects.

[6] While mineral dust aerosol influences climate, dust-induced changes in meteorological fields feed back to the dust cycle. Dust emissions decrease by 15–50% as a result of the reductions in surface wind speed associated with dust shortwave effect [*Perlwitz et al.*, 2001; *Miller et al.*, 2004a; *Perez et al.*, 2006; *Heinold et al.*, 2007]. Dust-induced changes in precipitation and turbulent mixing influence the deposition processes of dust aerosol, leading to changes in the lifetime of dust particles [*Miller et al.*, 2004a; *Ramanathan and Ramana*, 2005]. These studies underscored the importance of dust-climate coupling in simulations of the dust cycle and raised a question as to how the full dust-climate coupling influences simulated ultimate climate responses to dust radiative effects.

[7] The goal of this study is to examine the climate responses to shortwave and/or thermal radiative effects of dust aerosol using the Global transport Model of Dust (GMOD) embedded within a general circulation model. The model was developed and evaluated in the first part of this study [*Yue et al.*, 2009]. We focus especially on (1) longwave radiative effects of mineral dust and (2) climate responses to dust RF with two-way dust-climate coupling. The dust simulation and radiative transfer scheme will be described briefly in section 2. In section 3, the simulated annual mean, seasonal variation, and diurnal variation of the RF of dust are presented. Section 4 presents the climate responses to shortwave and/or longwave dust RF. Section 5 examines the effects of dust-climate coupling on the dust cycle and, consequently, on simulated climate responses.

2. Model Description and Numerical Experiments
2.1. Dust Simulation in the GMOD

[8] The GMOD is a global three-dimensional transport model of mineral dust aerosol embedded within the general circulation model IAP9L-AGCM [*Zeng et al.*, 1989; *Zhang*, 1990; *Liang*, 1996]. It has a horizontal resolution of $4° \times 5°$ and nine vertical levels and is coupled with a mixed layer ocean model [*Hansen et al.*, 1984]. The development of the GMOD is described and evaluated in part 1 of this work [*Yue et al.*, 2009]; we summarize here only the major features of the dust simulation in the GMOD.

[9] The whole dust size spectrum is divided into four bins (0.1–1.0, 1.0–2.0, 2.0–5.0, and 5.0–10.0 μm dry radius). A power law relation $n(r) \propto r^{-3}$ is used to describe the emitted dust size distribution, where r is radius of dust particle and $n(r)$ is the number density function. The uplift flux of dust is calculated as [*Wang et al.*, 2000]

$$Q_p = \begin{cases} C_1 C_2 s_p u_*^2 \left(1 - \dfrac{u_{*_t}}{u_*}\right)\left(1 - \dfrac{RH}{RH_t}\right) & u_* \geq u_{*_t} \quad \text{and} \quad RH \leq RH_t \\ 0 & \text{otherwise} \end{cases}$$

(1)

where Q_p is the uplift flux of particle size class p. C_1 is the potential emission coefficient of the soil, which does not incorporate the preferential sources but depends only on the vegetation types accounted for in the general circulation model (GCM), similar to the treatment by *Tegen and Fung* [1994]. C_2 is an empirical constant set to 2.9×10^{-11} obtained by the wind tunnel experiment [*Hu and Qu*, 1997], and s_p represents the fraction of dust mass in size bin p to total dust mass emitted. Meteorological factors that constrain dust emission in the GMOD are surface wind friction velocity u_* and relative humidity RH. Comparison using the National Centers for Environmental Prediction/National Center for Atmospheric Research (NECP/NCAR) reanalyses data [*Kalnay et al.*, 1996] shows that surface RH is closely related to soil moisture. Simulations by the GCM also show that the changes in surface RH are consistent with those in soil moisture. In this case, we use RH as a constraint for dust uplift instead of soil moisture which is widely used in other parameterizations [e.g., *Fécan et al.*, 1999; *Ginoux et al.*, 2001; *Lunt and Valdes*, 2002; *Zender et al.*, 2003]. RH_t and

u_{*t} are the threshold values for RH and u_*, respectively; dust particles can be blown into the atmosphere only when the surface wind speed u_* exceeds u_{*t} and relative humidity RH is smaller than RH$_t$. The threshold value u_{*t} has been reported to depend on soil particle size [*Iversen and White*, 1982; *Batt and Peabody*, 1999] and soil moisture [*Fécan et al.*, 1999; *Ginoux et al.*, 2001; *Woodward*, 2001; *Zender et al.*, 2003]. However, observations on a global scale are not available to evaluate our assumed thresholds. As a result, both u_{*t} and RH$_t$ are set to globally uniform constants, similar to that given by *Lunt and Valdes* [2002] and *Ginoux et al.* [2001].

[10] Dry deposition of dust is determined by the settling velocity, which considers the effects of both gravity and turbulence. Large particles generally have a large dry deposition velocity and cannot be transported far away from sources [*Tegen and Fung*, 1994]. The wet scavenging of dust is proportional to the precipitation rate, accounting for precipitation from both large-scale and convective clouds [*Woodward*, 2001; *Lunt and Valdes*, 2002].

[11] When driven by a mixed layer ocean model, the GMOD predicts a global dust emission of 1900 trillion gram (Tg) yr^{-1}, which is within the range of 200–5000 Tg yr^{-1} estimated in previous studies [*Tegen and Fung*, 1994; *Ginoux et al.*, 2001; *Zender et al.*, 2003; *Liao et al.*, 2004; *Cakmur et al.*, 2006]. The global and annual dry and wet depositions of dust are predicted to be 1279 Tg and 621 Tg, respectively. The predicted global dust burden is 27.0 Tg, and the average lifetime of dust particles is 5.2 days, which is comparable to results from other dust models [*Tegen and Lacis*, 1996; *Luo et al.*, 2003; *Zender et al.*, 2003].

2.2. Radiative Transfer Scheme

[12] The radiative transfer scheme in the GMOD follows that in the Community Climate Model 3 (CCM3) of the National Center for Atmospheric Research (NCAR) [*Yue and Wang*, 2009]. It uses a δ-Eddington approximation with 18 spectral intervals ranging from 0.2 to 5.0 μm [*Briegleb*, 1992] to calculate the shortwave radiation at each model hour. The scheme for longwave radiative transfer accounts for the absorptivity/emissivity of water vapor, carbon dioxide, ozone, and trace gases [*Ramanathan and Downey*, 1986].

[13] The radiative transfer scheme is updated to consider the radiative effect of dust. Dust optical thickness τ, single scattering albedo (SSA) ω, and asymmetry factor g are calculated using the Mie theory [*de Rooij and van der Stap*, 1984; *Mishchenko et al.*, 1999]. The dust refractive indices used in the GMOD are taken from the work of *Woodward* [2001] (cf. their Table 2), which were compiled on the basis of measurements at different locations. For longwave radiation, we employ an exponential transmission approximation for mineral dust aerosol [*Carlson and Benjamin*, 1980]

$$T_d^\lambda = \exp\left[-D \cdot \tau_d^\lambda\right] \qquad (2)$$

where D is a diffusivity factor that is set to 1.66, and τ_d is the optical depth of dust at a specific thermal wavelength λ. Since the thermal spectral interval is larger than the shortwave interval, each thermal wavelength band is divided into small subintervals, whose extinction coefficients are then weighted by the spectral intensity denoted as Planck function

$B(T, \nu)$. The extinction coefficient over the whole wave band λ can be calculated by *Zhang and Modest* [2002]

$$K_{ext}^\lambda = \frac{\sum_i k_i B(T, \nu_i) \Delta \nu}{\sum_i B(T, \nu_i) \Delta \nu} \qquad (3)$$

where k_i and ν_i are the extinction coefficient and the median wave number at each subinterval, respectively. The atmospheric transmission in the original scheme is then multiplied by the dust transmission to represent the perturbation of air transmission by dust.

2.3. Numerical Experiments

[14] To simulate the RF of mineral dust aerosols, we utilize the "double radiation call" method as described by *Woodward* [2001]. This method calls the radiation module twice in every radiation integration interval. In the first call, the dust radiative effects are considered, and the simulated radiative fluxes are output rather than progressed into the model. The radiation module is then called for the second time without the dust effects, and the results of this call are used as the updated atmospheric radiative state of the GCM. The climatology of the GCM is not perturbed by dust. The RF of dust is obtained by the differences in radiative fluxes of the two calls.

[15] Next, new climate simulations are conducted to examine the climatic effect of mineral dust aerosol:

[16] 1. The CTRL run gives the simulation of present-day climate and dust cycle. Simulated climate is one-way coupled with the simulation of dust cycle; meteorological fields are used to drive the simulation of dust cycle, but the radiative effect of dust is not allowed to feedback into the GCM climate. Simulated dust cycle quite resembles that given by *Yue et al.* [2009], which is obtained by driving the climate model with fixed sea surface temperature (SST).

[17] 2. The simulation FIXDST gives the simulation of the effect of dust on present-day climate. Optical properties of dust are calculated based on offline monthly concentrations of dust from the CTRL simulation and fed back into the GCM climate. Dust concentrations do not vary with simulated climate.

[18] 3. The simulation CPLD gives the simulation of present-day climate and dust cycle. Simulated climate is two-way coupled with the simulation of dust cycle; meteorological fields are used to drive the simulation of dust cycle, and the radiative effect of dust is fed back into the GCM climate.

[19] Differences in climate between FIXDST and CTRL represent climatic effect of dust with noninteractive dust cycle. The differences between CPLD and CTRL show the effect of full climate-dust coupling on simulated dust cycle, and those between CPLD and FIXDST assess the effect of climate-dust coupling on simulated climate. To quantify the roles of the shortwave and longwave direct radiative effect (DRE) of dust, each of FIXDST and CPLD includes three simulations. In experiments with the subscript "SW" (such as FIXDST$_{SW}$ and CPLD$_{SW}$), only the shortwave DRE of the dust aerosols is considered in the radiative transfer scheme of the GCM. Similarly, only the thermal effect of dust is considered in FIXDST$_{LW}$ and CPLD$_{LW}$. Both longwave and shortwave effects of dust are considered in

Table 1. Summary of Numerical Experiments[a]

Experiments	Simulation of Dust Cycle	Dust Shortwave DRE in GCM Climate	Dust Longwave DRE in GCM Climate	Interactive Dust-Climate
CTRL	√			
FIXDST_ALL		√	√	
FIXDST_SW		√		
FIXDST_LW			√	
CPLD_ALL	√	√	√	√
CPLD_SW	√	√		√
CPLD_LW	√		√	√

[a]DRE, direct radiative effect; GCM, general circulation model.

FIXDST_ALL and CPLD_ALL. All the simulations are summarized in Table 1.

[20] Simulations FIXDST and CPLD are equilibrium climate simulations; each simulation is integrated for 50 years. The mean values of the last 30 years from these simulations are analyzed and discussed in the following sections.

3. Radiative Forcing of Dust

3.1. Dust Optical Thickness

[21] The predicted seasonal mean dust optical thickness (DOT) values at 0.55 μm are shown in Figure 1. The values of exceeding 0.05 are found over northern Africa throughout the year and over almost entire Asia in June−July−August (JJA). DOT values are predicted to be the lowest in December−January−February (DJF). Such seasonal variation of DOT is associated with that of predicted dust burden,

which has been evaluated by *Yue et al.* [2009]. The GMOD generally captures the seasonal variation of global dust transport, except that the model underestimates dust concentrations in Asia in March−April−May (MAM) [*Yue et al.*, 2009]. The simulated annual and global mean DOT is 0.032; this value is close to 0.030 estimated by *Tegen and Lacis* [1996] and 0.037 by *Liao et al.* [2004], both of which were obtained using global models.

3.2. Dust Radiative Forcing

[22] Predicted global distributions of solar, thermal, and net RF (shortwave plus longwave) of mineral dust aerosol are shown in Figure 2. The solar RF is negative at the surface because of the scattering and absorption of sunlight by dust particles and positive at the top of the atmosphere (TOA) over the high-albedo Sahara Desert (Figures 2a and 2b). The longwave RF is positive throughout the atmosphere (Figures 2c and 2d), with maximum forcing at the surface. The net RF is a cooling at the surface, while at the TOA, it is warming over land but cooling over oceans (Figures 2e and 2f). Such pattern in net RF agrees with that found by *Ackerman and Chung* [1992], *Woodward* [2001], and *Liao et al.* [2004]. The vertical distribution of RF over the Sahara Desert can be seen in Figure 3, which is a cross section along 22°N. The shortwave RF changes sign at about 550 hPa altitude. Since radiative heating rate is determined by the vertical gradient of radiative fluxes in the atmosphere, the increase of net RF with the increase of height in Figure 3 indicates that dust particles cause heating throughout the entire column. Such great absorption is consistent with the
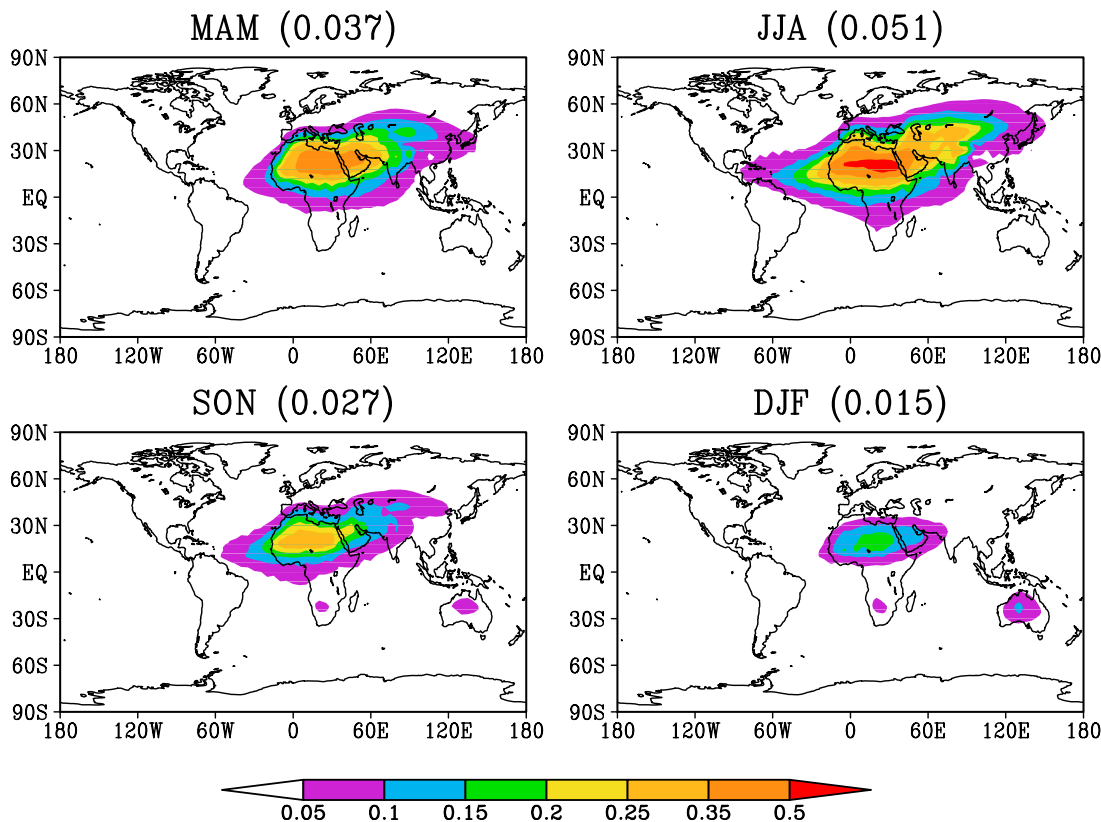

Figure 1. Simulated seasonal mean dust optical thickness (DOT) at 0.55 μm. The global mean DOT for each season is given in brackets.
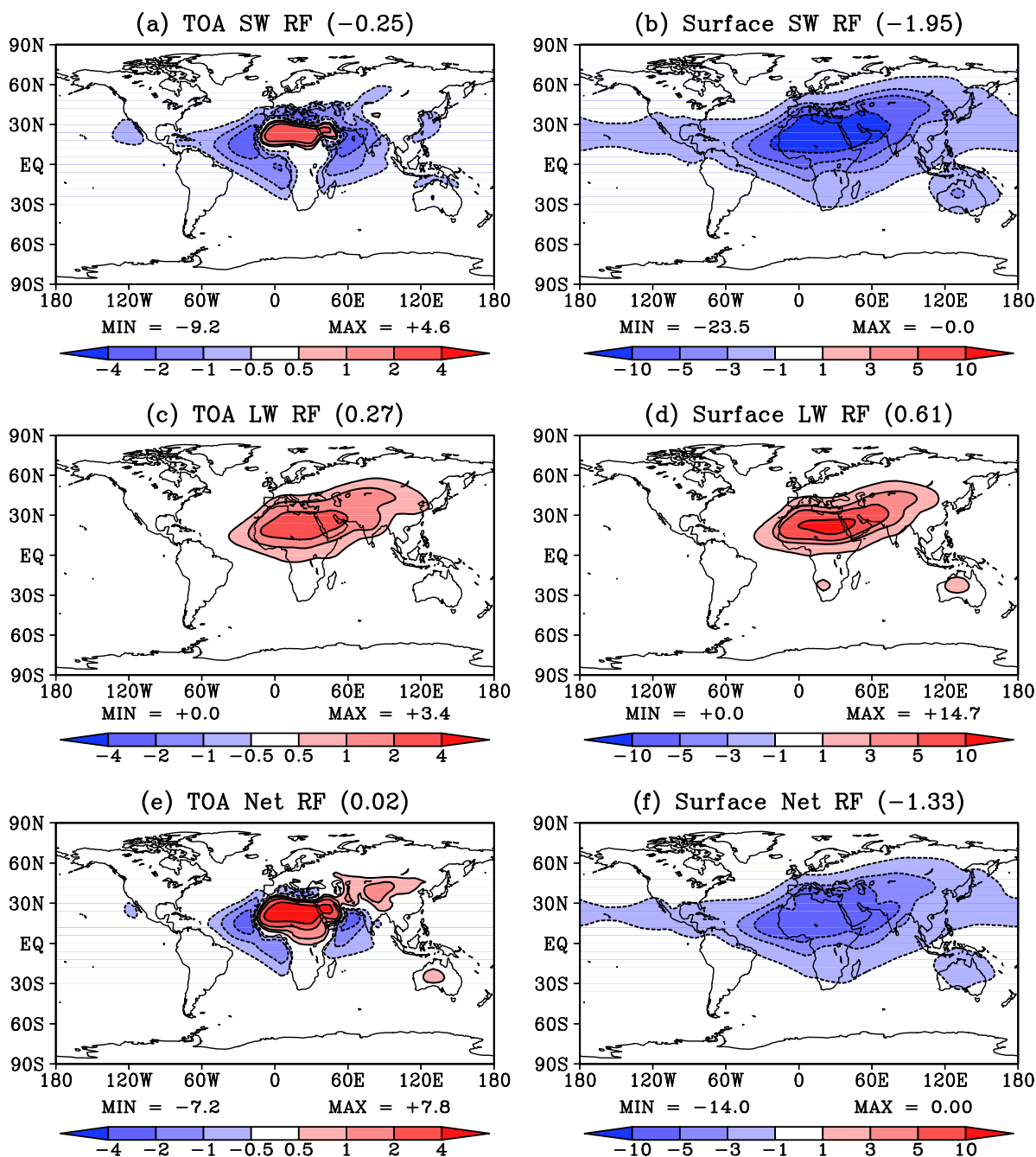
Figure 2. Simulated annual mean all-sky radiative forcings (RF) of mineral dust aerosol. (a) Shortwave RF at top of the atmosphere (TOA); (b) shortwave RF at the surface; (c) longwave RF at TOA; (d) longwave RF at the surface; (e) net RF at TOA; (f) net RF at the surface. The global mean RF is indicated in brackets for each panel. Positive values (solid contours) indicate increases of downward radiation. Units: W m^{-2}.

low single scattering albedo (SSA) of about 0.89 at 0.55 μm for the Saharan dust in the GMOD.

[23] The predicted contributions of different size bins to the total dust RF are shown in Table 2. The mass percentages of the four dust bins in the GMOD are 20%, 30%, 39%, and 11%, respectively. In the first size bin with the smallest particles, shortwave RF values are negative at both TOA and the surface. For particles larger than 1 μm, solar RF values at TOA are positive. As a result, the heating over the

Sahara Desert in Figure 2a can be explained by both the high surface albedo and the relatively large fraction of coarse particles ($r > 1.0$ μm) over the dust source region. At the surface, shortwave cooling decreases with the increase in particle radius. Although particles in the first dust bin account for only 1/5 of total dust mass, they contribute about 1/2 of the surface cooling. For the longwave RF, particles in the size bin of 2–5 μm are predicted to have the largest contribution to total longwave forcing.
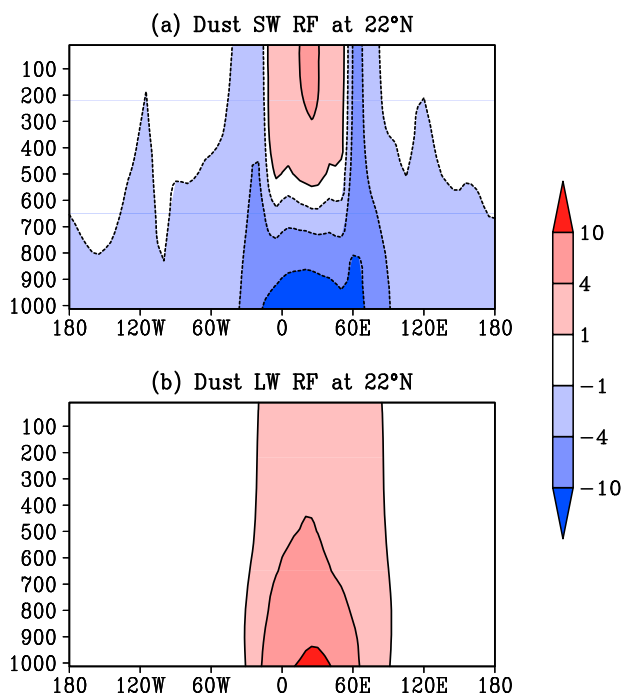
Figure 3. Vertical distributions of simulated annual mean dust RF along 22°N. (a) Shortwave RF; (b) longwave RF. Positive values (solid contours) indicate increases of downward radiation. Units: W m^{-2}.

[24] The simulated annual and global mean RF of mineral dust aerosol in this work is compared with results from previous studies in Figure 4. The models agree with each other that the longwave RF values are positive at both the TOA and the surface and the shortwave RF values at the surface are always negative. However, the sign of shortwave RF at TOA differs in different models (Figure 4a), indicating the large uncertainties which can be attributed to the differences in simulated dust burdens, assumed refractive indices, air temperature profiles, and so on [*Penner et al.*, 2001; *Forster et al.*, 2007]. At the TOA, the GMOD simulated shortwave and longwave RF values are −0.25 W m^{-2} and +0.27 W m^{-2}, respectively, which are close to the averaged shortwave RF of −0.33 W m^{-2} and the averaged longwave RF of +0.19 W m^{-2} from previous models. At the surface, the global and annual mean RF is −1.95 W m^{-2} in solar bands and +0.61 W m^{-2} in thermal bands in the GMOD, which are comparable to the average shortwave RF of −1.60 W m^{-2} and the average longwave RF of +0.44 W m^{-2} obtained in previous studies. The simulated net RF in the GMOD is +0.02 W m^{-2} at the TOA and −1.33 W m^{-2} at the surface.

[25] Table 3 shows the seasonal variation of the global mean dust RF in the GMOD. The RF at both the TOA and surface are the strongest in JJA, as a result of the largest dust burden predicted in this season. The RF of dust aerosol also has a distinct diurnal variation, as shown in Figure 5. Figures 5a–5d are the annual mean of the net RF at 0000, 0600, 1200, and 1800 model hours UT, respectively. The net RF at the surface is always cooling in areas with sunlight and warming in areas at nighttime, although the annual mean net RF is a cooling globally (Figure 2f). Such

diurnal variation of dust RF is a unique feature of dust forcing.

4. Climate Responses to RF of Dust

4.1. Temperature

4.1.1. Annual Mean Responses in Air Temperature

[26] Figures 6a–6d show predicted responses of air temperature to dust shortwave RF (differences between FIXDST$_{SW}$ and CTRL) at different vertical layers. At the surface, the solar DRE of dust leads to reductions of surface air temperature (SAT) over the Sahara Desert and the oceans (Figure 6a). The largest cooling of 0.9 K is predicted over the central desert. SAT is predicted to increase over Eurasia and the United States, because of the dust-induced reductions in cloud cover (Figure 9b) that allow more solar radiation to reach the ground. The global and annual mean SAT is predicted to be reduced by 0.07 K by shortwave RF of dust. Over the Sahara Desert, the shortwave cooling weakens as the altitude increases. The area of cooling is predicted to decrease at 850 mb (Figure 6b), and a large area of warming is predicted in the mid-high latitudes in the Northern Hemisphere (NH) at 500 hPa (Figure 6c). A general warming is predicted at mid-high latitudes in both hemispheres at 200 hPa, with a global and annual mean increase in temperature of 0.03 K.

[27] The responses in temperature to the longwave RF of dust are shown in Figures 6e–6h. Relative to the CTRL simulation, SAT in FIXDST$_{LW}$ shows a maximum increase of 1.2 K over the Sahara Desert (Figure 6e). Over the oceans, dust thermal RF leads to a general warming that extends from the surface to the upper troposphere (Figures 6e–6h).

[28] The changes in temperature profiles in FIXDST$_{SW}$ and FIXDST$_{LW}$ are also a result of the feedback of SST. The negative shortwave perturbation at the surface reduces SST, which reduces evaporation and the vertical transport of water vapor (not shown). On the other hand, dust thermal DRE increases SST and evaporation over the oceans, increasing atmospheric water vapor content. Since water vapor is an important greenhouse gas, air temperature over the tropical oceans shows reductions in Figures 6a–6d and increases in Figures 6e–6h.

[29] Figures 6i–6l show predicted responses of air temperature to net dust RF at different vertical layers. Over continents (Figure 6i), dust aerosol causes surface warming almost everywhere in the NH except for southeastern China, South Asia, and western Europe; maximum warming of exceeding 0.8 K is predicted over the central Sahara Desert. The net RF of dust aerosol is predicted to lead to cooling

Table 2. Simulated Annual Global Mean Dust RF for Different Size Bins[a]

Dust Radius	TOA			Surface		
	SW	LW	Net	SW	LW	Net
0.1–1.0 μm	−0.45	+0.06	−0.39	−0.97	+0.06	−0.91
1.0–2.0 μm	+0.03	+0.09	+0.12	−0.57	+0.16	−0.41
2.0–5.0 μm	+0.14	+0.10	+0.24	−0.38	+0.32	−0.06
5.0–10.0 μm	+0.04	+0.01	+0.05	−0.06	+0.08	+0.02
0.1–10.0 μm	−0.25	+0.27	+0.02	−1.95	+0.61	−1.34

[a]Positive values indicate increases of downward radiation. Units: W m^{-2}. TOA, top of the atmosphere; SW, shortwave; LW, longwave.
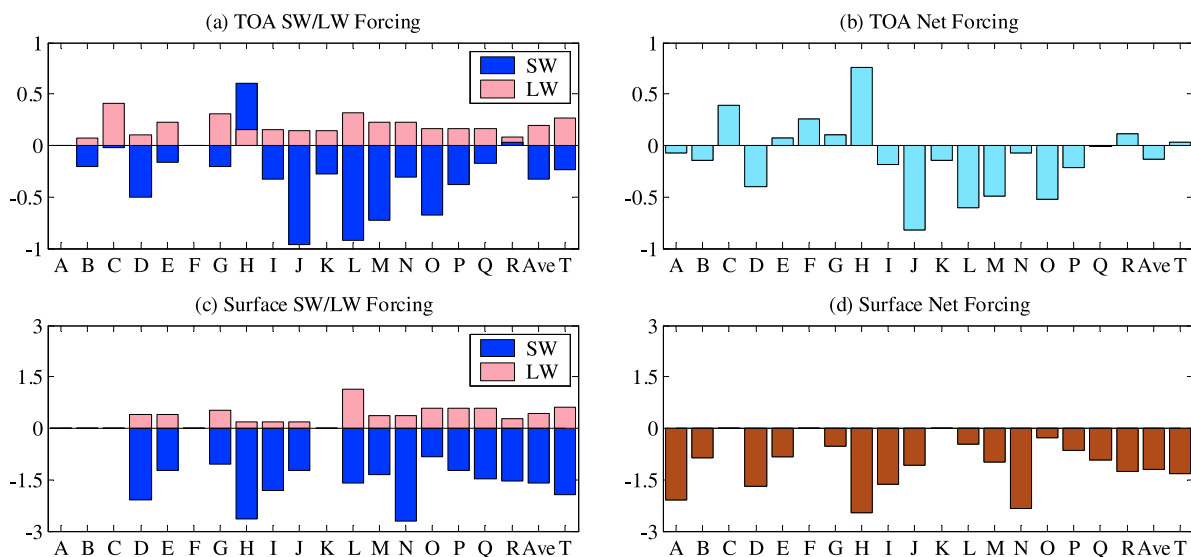
Figure 4. Comparison of annual and global mean radiative forcing of mineral dust estimated in different studies. (a) Shortwave and longwave RF at TOA; (b) net RF at TOA; (c) shortwave and longwave RF at surface; (d) net RF at surface. Positive values indicate increases of downward radiation. Units: W m^{-2}. Symbols in the horizontal axis refer to previous studies as follows: A, *Miller and Tegen* [1998]; B, *Jacobson* [2001]; C, *Myhre and Stordal* [2001]; D, *Perlwitz et al.* [2001]; E, *Woodward* [2001]; F, *Takemura et al.* [2002]; G, *Liao et al.* [2004]; H, *Miller et al.* [2004b] (0.9 × ω); I, *Miller et al.* [2004b]; J, *Miller et al.* [2004b] (1.1 × ω); K, *Reddy et al.* [2005]; L, *Yoshioka et al.* [2007]; M, *Shell and Somerville* [2007] (ω = 0.97); N, *Shell and Somerville* [2007] (ω = 0.85); O, *Tanaka et al.* [2007] (ADEC-1); P, *Tanaka et al.* [2007] (ADEC-2); Q, *Tanaka et al.* [2007] (OPAC-MD); R, *Tanaka et al.* [2007] (dust-like); Ave, average of above; T, this study.

over oceans. Since the warming effect in some areas offsets cooling in other places, the net RF leads to no change in global mean SAT (Figure 6i). At 850 hPa (Figure 6j), the area of warming extends to oceans in the midlatitudes and high latitudes in the NH. The net effect of warming is the most significant at higher layers; a global and annual mean warming of 0.12 K is predicted at 200 hPa (Figure 6l).

[30] In comparison to the SAT responses to the net RF simulated in other studies, there are both similarities and differences. Both *Miller and Tegen* [1998] and *Shell and Somerville* [2007] predicted a small reduction in the global mean SAT in the presence of dust aerosol. However, *Weaver et al.* [2002] showed that SAT increases by about 1 K over the Sahara Desert when considering the dust RF. Outside the source regions, we predict increases in SAT over North America and central Asia, which agrees with the results of *Overpeck et al.* [1996]. The differences in SAT response among different studies can be attributed to the differences in dust size distribution, vertical profile, and refractive index. However, the dust-induced increases in air temperature at high levels (above 850 hPa) have been found by both observations [*Alpert et al.*, 1998; *Satheesh et al.*, 2007] and simulations [*Carlson and Benjamin*, 1980; *Weaver et al.*, 2002; *Kim et al.*, 2006].

4.1.2. Diurnal Responses in Surface Air Temperature

[31] As a result of the diurnal variation in dust RF shown in Figure 5, responses in SAT at different model hours (Figure 7) also exhibit diurnal changes. Because the thermal RF of dust exists throughout a day while the solar RF works only in the presence of sunlight, SAT shows reductions in the daytime (Figures 7c and 7d), and the positive net DRE

at night leads to an increase in SAT over the Sahara Desert (Figures 7a and 7b). One interesting feature is the cooling of about −0.14 K over the Sahara Desert at 1200 UT. It is a cooling there even with longwave RF, a feature that cannot be seen in the annual mean plot with net forcing (Figure 6i). At local 0000 (Figure 7a), heating over the Sahara Desert is 0.44 K stronger than the annual mean. On an annual mean basis, the changes in diurnal, daytime (local 0900–1600), and nighttime (local 2100–0400) mean surface air temperature are predicted to be +0.32 K, −0.11 K, and +0.68 K, respectively, in the FIXDST simulation. This simulated diurnal variation of the dust-induced changes in SAT is consistent with the cooling by day and warming by night measured by *Washington et al.* [2006] (cf. their Figure 6).

4.2. Surface Energy Balance

[32] Figure 8 presents the changes in the surface latent and sensible heat fluxes in the presence of dust (differences

Table 3. Simulated Seasonal Global Mean RF of Dust Aerosol[a]

	DJF	MAM	JJA	SON
TOA:				
SW	−0.13 (−4.4)	−0.24 (−12.6)	−0.36 (−13.8)	−0.26 (−5.7)
LW	+0.10 (1.1)	+0.33 (4.5)	+0.46 (6.1)	+0.20 (2.4)
Surface:				
SW	−0.87 (−10.0)	−2.28 (−32.7)	−3.13 (−38.1)	−1.52 (−16.8)
LW	+0.29 (6.6)	+0.79 (18.3)	+0.92 (24.5)	+0.45 (11.2)

[a]Positive values indicate increases of downward radiation. For the positive (negative) values, the regional maximum (minimum) is shown in brackets. Units: W m^{-2}. DJF, December–January–February; MAM, March–April–May; JJA, June–July–August; SON, September–October–November.
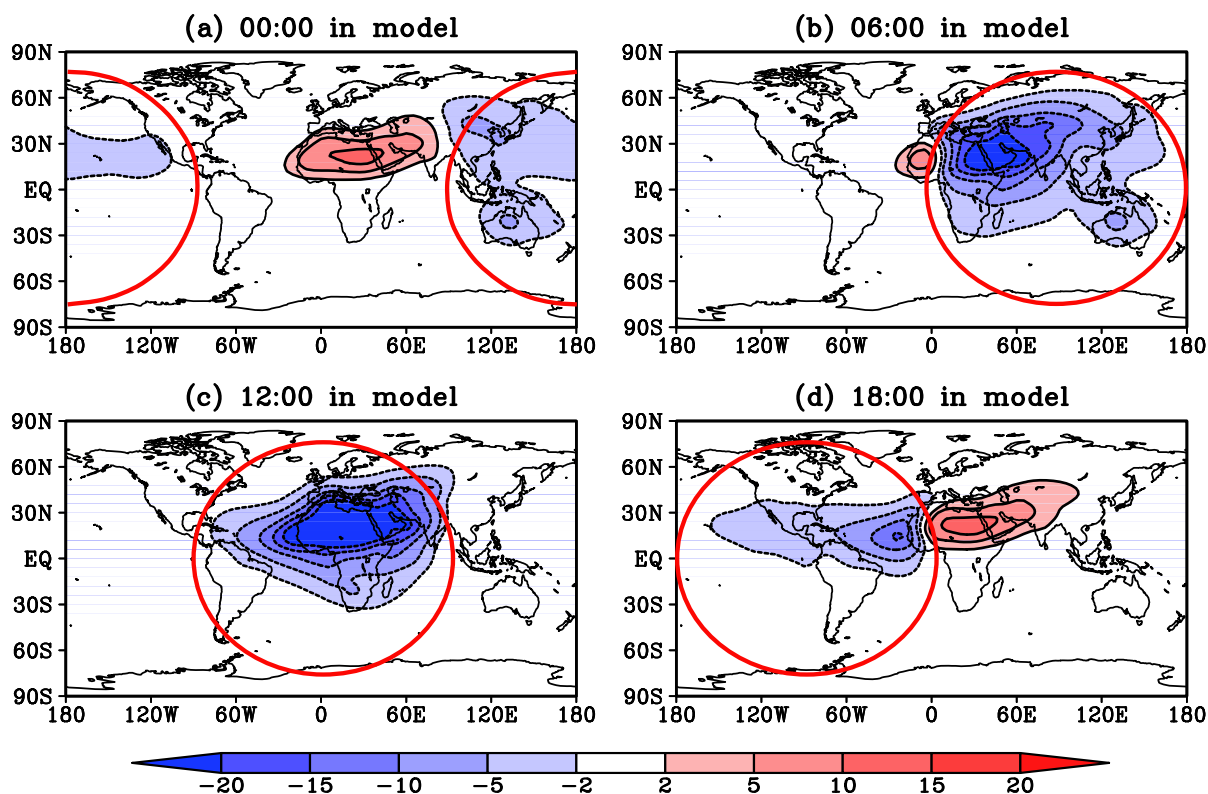
Figure 5. Simulated annual mean net surface RF (shortwave plus longwave) of dust aerosols at model hours of (a) 0000, (b) 0600, (c) 1200, and (d) 1800 UT. The red circle represents the domain with insolation in the general circulation model (GCM). Positive values (solid contours) indicate increases of downward radiation. Units: W m^{-2}.

between FIXDST$_{ALL}$ and CTRL). The latent heat flux increases over central Africa (Figure 8a) by anomalous increase in local precipitation (Figure 9c), similar to the results given by *Miller et al.* [2004b]. On the other side, the latent heat decreases over the oceans near the Sahara Desert, reflecting the decreases in SST and corresponding reductions in evaporation. The distribution of the changes in surface latent heat flux in Figure 8a is quite similar to the prediction by *Miller et al.* [2004b] (cf. their Figure 14a). The global and annual mean latent heat flux decreases by 0.59 W m^{-2} in the presence of dust aerosol.

[33] Dust aerosol also decreases the sensible heat flux from the surface to the atmosphere, especially over the Sahara Desert (Figure 8b). The sensible heat depends both on the contrast of ground-air temperature and the turbulent energy [*Liu et al.*, 2004]. The daytime cooling at the surface leads to reductions in the upward transport of heat from the surface to the atmosphere. On the other side, the warming at night increases the upward transport of sensible heat. Since the turbulence is much more active in the daytime than in the nighttime [*Liu et al.*, 2004], the daytime decrease exceeds the nighttime increase of sensible heat from surface to atmosphere, leading to a net decrease in the global annual mean sensible heat flux of 0.52 W m^{-2}.

[34] The decreases in global and annual mean surface latent heat and sensible heat fluxes by dust aerosol have been found in previous studies which account for both shortwave and longwave RF [*Miller et al.*, 2004b; *Shell and Somerville*, 2007]. Such changes help to constrain the

dust-induced surface cooling to a certain level. With shortwave RF alone (FIXDST$_{SW}$-CTRL), the global and annual mean latent and sensible heat fluxes are predicted to decrease by 0.76 W m^{-2} and 0.70 W m^{-2}, respectively (Table 5). The magnitude of these changes is larger than that in FIXDST$_{ALL}$. On the other side, in FIXDST$_{LW}$, the global annual mean latent and sensible heat increase by 0.29 W m^{-2} and 0.17 W m^{-2}, respectively, relative to CTRL simulation (Table 5). These results indicate that the thermal DRE of dust partly offsets the changes in surface energy induced by the solar DRE.

4.3. Hydrological Cycle

[35] Figure 9 shows the responses of hydrological cycle to the DRE of dust (differences between FIXDST$_{ALL}$ and CTRL). At the surface, the specific humidity of the surface air (QAS) has a widespread increase over the Sahara Desert, the Arabian Peninsula, eastern China, and the United States (Figure 9a). QAS over the central Atlantic and the Indian Ocean is predicted to decrease. On a global and annual mean basis, the DRE of dust causes an increase of 0.01g kg^{-1} in surface humidity. Such changes in QAS are closely related to the changes in SAT. Generally, the increases in SAT increase evaporation, leading to increases in QAS and vice versa. As a result, the pattern of the changes in QAS (Figure 9a) is quite similar to that of the changes in SAT (Figure 6i).

[36] Figure 9b shows the predicted changes in middle cloud amount (MCA). The MCA decreases over Northern Africa, central Asia, and eastern China. Such reductions are
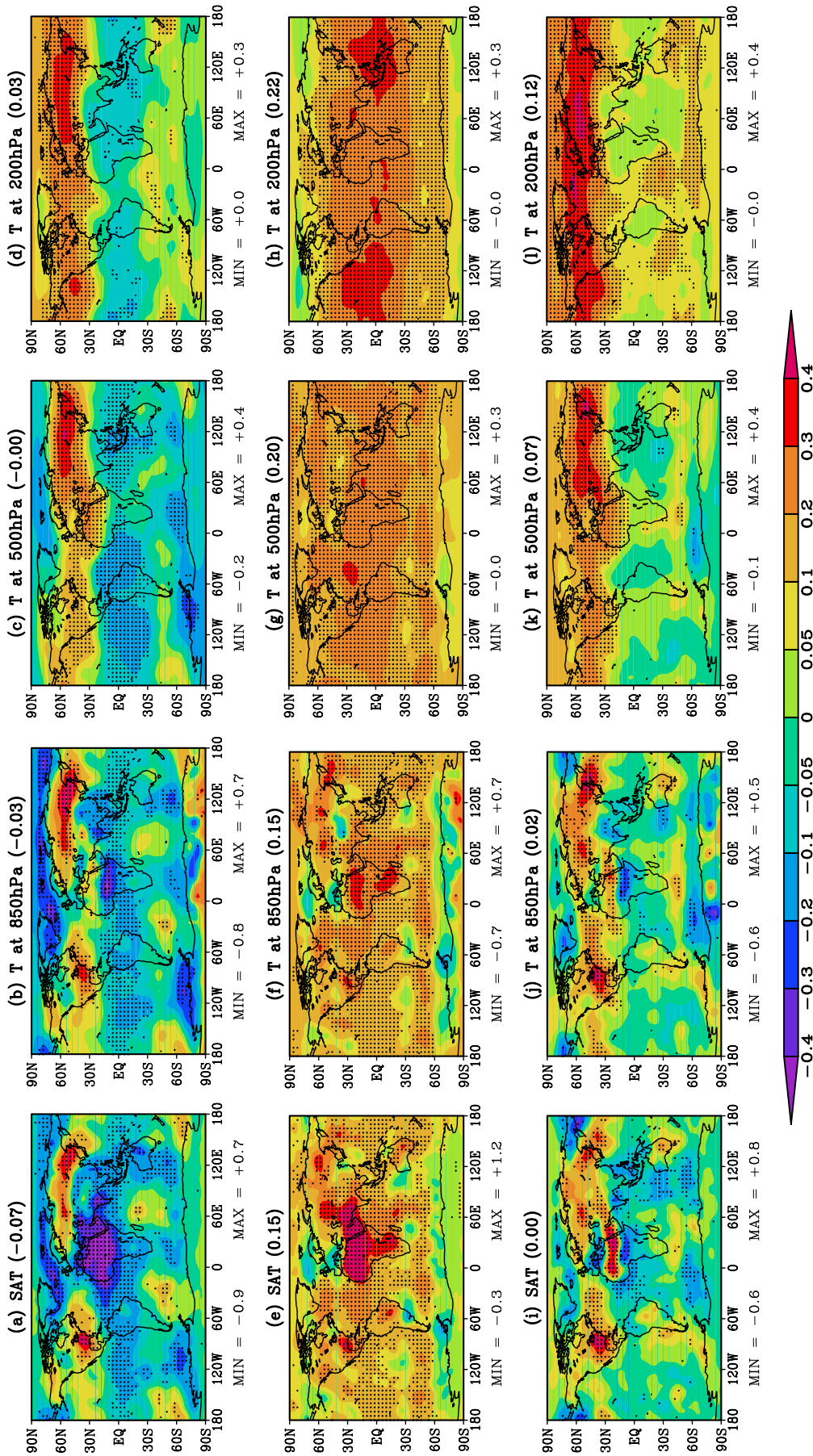
Figure 6. Simulated annual mean changes in air temperature at surface, 850 hPa, 500 hPa, and 200 hPa in the presence of dust aerosol. The effects of (a–d) shortwave RF (FIXDST$_{SW}$–CTRL), (e–h) longwave RF (FIXDST$_{LW}$–CTRL), and (i–l) net RF (FIXDST$_{ALL}$–CTRL) are shown. The differences that pass the 95% significance level are denoted with dots. Units: K.
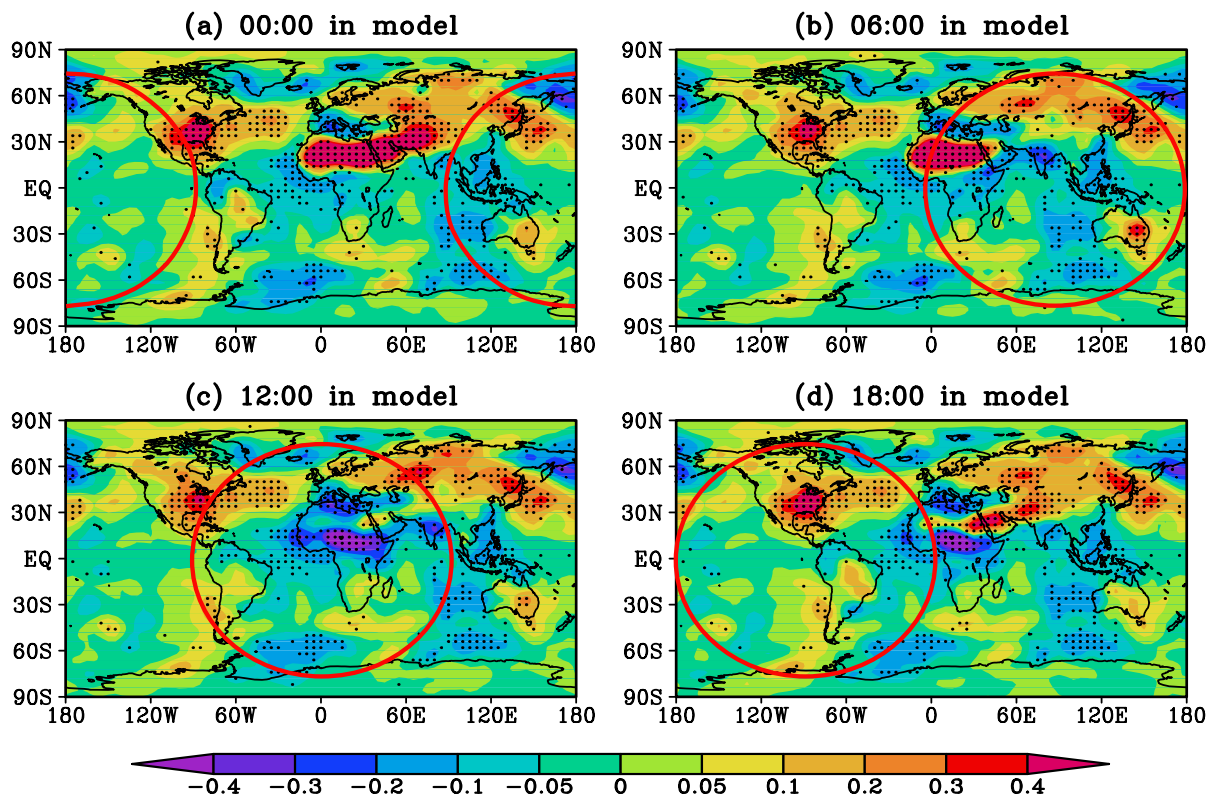
Figure 7. Simulated annual mean changes in surface air temperature (SAT) in the presence of dust at (a) 0000, (b) 0600, (c) 1200, and (d) 1800 model hours UT (FIXDST$_{ALL}$-CTRL). The red circle represents the domain with insolation in the GCM. The differences that pass the 95% significance level are denoted with dots. Units: K.

closely related to the changes in air temperature by dust DRE. As the dust-induced warming becomes stronger in the upper layers (Figures 6i–6l), atmospheric stability increases, and fewer clouds can form. On a global scale, MCA and total cloud amount (TCA) (not shown) reduce by 0.13% and 0.08%, respectively. Our results agree with those by *Perlwitz et al.* [2001], which predicted a decrease in the total cloud amount in a dust-climate interactive model with both long-wave and shortwave RF of dust.

[37] The changes in surface latent heat flux and cloud amount result in the changes in rainfall. Figure 9c shows that precipitation decreases in most places, especially over the Atlantic Ocean. However, in central Africa, dust leads to an anomalous increase in local precipitation. Such anomaly is probably attributed to the radiation absorption by dust, which may be large enough to change the sign of diabatic heating within the atmospheric column and lead to increase in precipitation [*Menon et al.*, 2002]. The pattern of the rainfall anomaly is similar to the results of *Miller et al.* [2004b] (cf. their Figure 16). On a global scale, dust leads to a reduction of 0.02 mm d^{-1} in precipitation. Note that the indirect effect of dust is not considered in this work; the indirect effect may affect precipitation more significantly [*Kaufman et al.*, 2005].

[38] The hydrological cycle shows different responses to the solar and thermal DRE of dust. In FIXDST$_{SW}$, the cloud amount and the precipitation exhibit reductions similar to those in FIXDST$_{ALL}$. However, in FIXDST$_{LW}$, both the MCA and TCA show modest changes (Table 5). The columnar warming (Figures 6e–6h) in FIXDST$_{LW}$ causes small changes in the atmospheric stability, leading to small changes in the middle and total cloud amount as a result.

4.4. Surface Wind Speed

[39] Figure 10 shows the dust-induced changes in friction velocity (differences between FIXDST$_{ALL}$ and CTRL). The wind speed is predicted to increase over northern Africa and the Arabian Peninsula. The increases in SAT in these areas (Figure 6i) enhance air temperature lapse rate (not shown), decrease air stability, and facilitate anomalous vertical uplift as a result. On the basis of mass continuity, the surface horizontal wind velocity is then reinforced. These predictions in our work are different from results of *Miller et al.* [2004a], which simulated reductions in surface wind speed with both longwave and shortwave RF. The reason for the difference is that surface temperature was predicted to decrease by *Miller et al.* [2004a], which reduces the turbulent flux of sensible heat back into the atmosphere. However, *Heinold et al.* [2007] simulated both increase and decrease of surface wind speed in response to dust net RF at different locations. Such results show the complexity of dust climatic effect.

5. Importance of Dust-Climate Interactions

5.1. Effects of Dust-Climate Two-Way Coupling on Simulated Dust Cycle

[40] The dust-induced changes in meteorological fields will influence the emission and transport of dust particles in
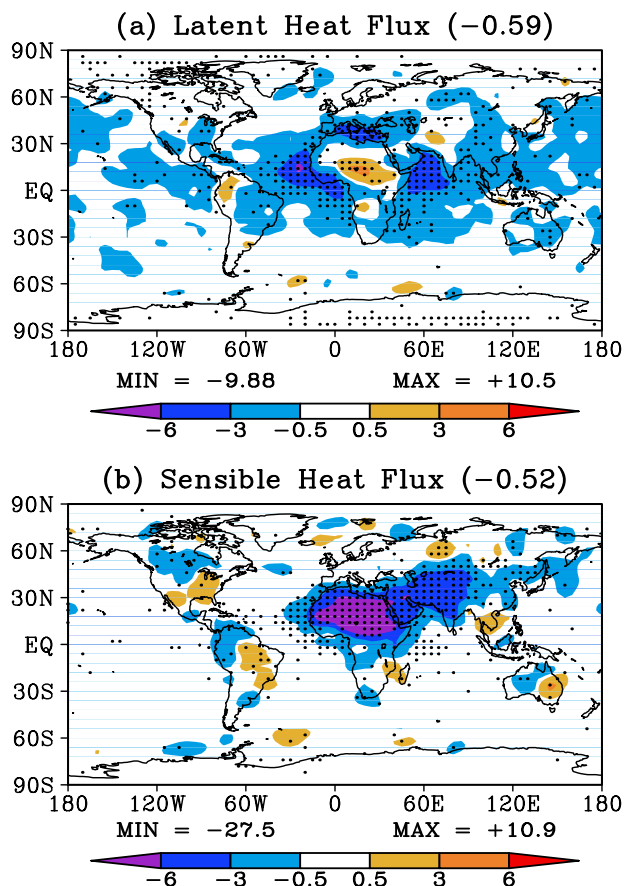
Figure 8. Predicted annual mean changes in (a) latent heat flux and (b) sensible heat flux in the presence of dust aerosol (FIXDST$_{ALL}$-CTRL). Positive values indicate increases of upward flux. The differences that pass the 95% significance level are denoted with dots. Units: W m^{-2}.

return. Effects of dust-climate two-way coupling on simulated dust cycle are estimated as the differences in simulated dust cycle between CPLD simulations and the CTRL run. Table 4 summarizes emission, dry/wet deposition, burden, average lifetime, and DOT obtained in different experiments. The dust cycle in the CPLD$_{ALL}$ run differs from that simulated in the CTRL simulation in the following aspects. First, the dust uplift in CPLD$_{ALL}$ is lower by approximately 2%, as a result of the increases in humidity in dust source region (Figure 9a). The responses in meteorological fields to dust RF lead to smaller changes in dust emissions in our work than in other studies. *Perlwitz et al.* [2001] estimated a 15% reduction in annual dust emission with an interactive model, and *Heinold et al.* [2007] reported a reduction in dust emission of up to 50% during a dust event. The modest change in dust uplift in our simulation can be explained by the predicted increases in the surface wind speed over dust source regions (Figure 10), which partly counteract the effect of increased surface humidity. Second, predicted dust burden is higher by 13% in CPLD$_{ALL}$, although the changes in dust uplift are very small relative to the CTRL run. Wet deposition of dust becomes less effective when precipitation decreases in CPLD$_{ALL}$. Third, the average dust lifetime increases by

about 15%. The reduction in rainfall (or wet deposition of dust) mainly occurs outside source regions (Figure 9c), where small particles dominate. Small particles contribute greatly to shortwave RF; the elongation of their lifetime will enhance dust shortwave DRE.

[41] Table 4 also shows the changes in dust cycle in CPLD$_{SW}$ and CPLD$_{LW}$ relative to the CTRL run. In CPLD$_{SW}$, the total dust uplift decreases by 5% while the
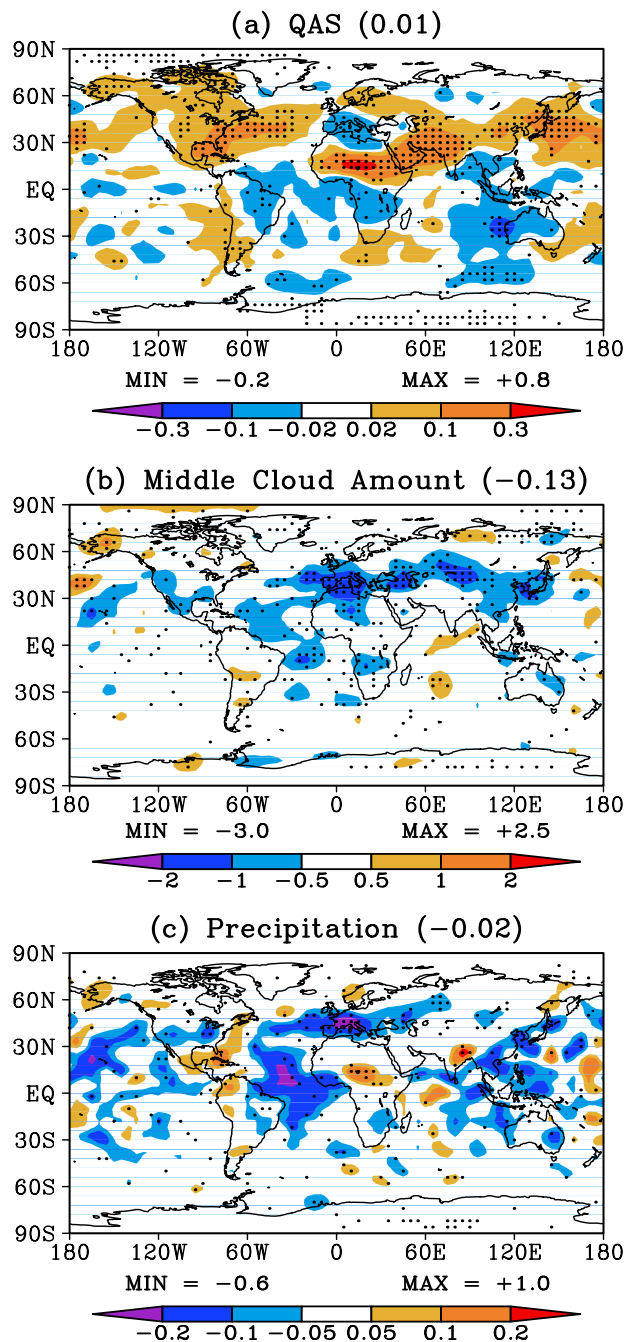

Figure 9. Predicted annual mean changes in the hydrological cycle in the presence of dust aerosol (FIXDST$_{ALL}$-CTRL). (a) Specific humidity of the surface air (QAS), units: g kg^{-1}; (b) middle cloud amount, units: %; (c) precipitation, units: mm d^{-1}. The differences that pass the 95% significance level are denoted with dots.
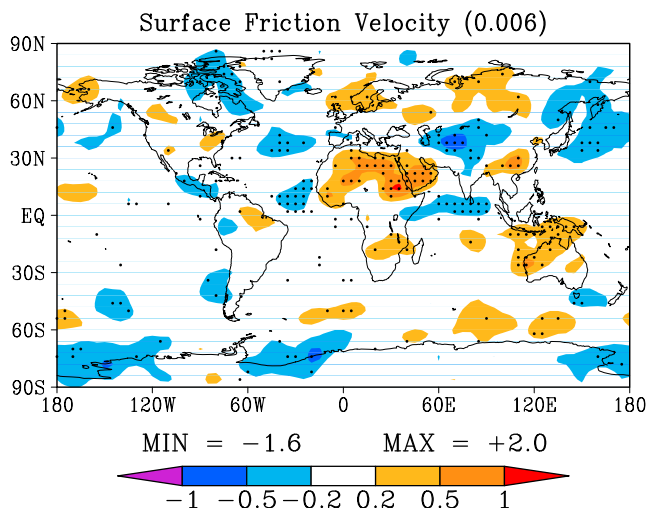
Figure 10. Predicted annual mean changes in surface friction velocity in the presence of dust aerosol (FIXDST$_{ALL}$-CTRL). The differences that pass the 95% significance level are denoted with dots. Units: cm s^{-1}.

dust loading increases by 9%. As a result, the average lifetime of dust increases to 6 days. The annual dust emission in CPLD$_{LW}$ increases by 6%, and the dust burden also increases by a similar magnitude, indicating that the increase in dust loading in CPLD$_{LW}$ is mainly attributed to the intensification of the source strength.

[42] The main factors that influence dust mobilization are the relative humidity and the wind velocity at the surface (equation (1)). Figure 11 compares the changes in relative humidity at 2 m (RH2) and friction velocity (UVR) in CPLD$_{SW}$ and CPLD$_{LW}$ relative to the CTRL simulation. RH2 increases and UVR decreases over the Sahara Desert in CPLD$_{SW}$ (Figures 11a and 11b), while RH2 decreases and UVR increases in CPLD$_{LW}$ (Figures 11c and 11d), which explains the changes in emissions in CPLD$_{SW}$ and CPLD$_{LW}$ relative to the CTRL run.

[43] The dust-induced changes in meteorological fields will also feed back into the diurnal cycle of dust uplift. *Yue et al.* [2009] showed that dust uplift is the largest in the daytime, and the ratio of the daily maximum emission to the minimum can reach as high as 75 on a global and annual basis. With dust-climate coupling, this diurnal cycle is weakened. The surface cooling by shortwave DRE of dust reduces dust emissions in the daytime, and the increase in SAT by dust thermal DRE increases dust emissions at night. As a result, the ratio of the maximum uplift to the minimum is predicted to decrease to 41. This result indicates that dust-climate interaction is important in simulations of diurnal cycle of dust.

5.2. Effects of Dust-Climate Two-Way Coupling on Simulated Climate

[44] Effects of dust-climate two-way coupling on simulated climate are estimated by the differences in simulated climate between CPLD and FIXDST simulations. Figure 12 shows the differences in air temperature response between CPLD$_{ALL}$ and FIXDST$_{ALL}$. Relative to the air temperatures in FIXDST$_{ALL}$ (Figures 6i–6l), the dust cooling effect is strengthened in CPLD$_{ALL}$ as a result of full dust-climate

coupling. At each level, CPLD$_{ALL}$ predicts stronger cooling of about 0.05 K than FIXDST$_{ALL}$ on a global mean basis.

[45] The differences between the noninteractive and interactive experiments are determined by two factors. One is the change in dust climatology. The global dust burden increases by approximately 13% in CPLD$_{ALL}$ relative to the CTRL simulation (Table 4), with the mass in the smallest size bin increased by 20%. The other factor is the change in diurnal cycle of dust. As mentioned above, dust emission is the most active during daytime and relatively inactive during nighttime [*Yue et al.*, 2009]. Accounting for such diurnal variation in CPLD$_{ALL}$ enhances shortwave RF of dust. Our sensitivity studies indicate that the former and the latter factors contribute to about 80% and 20% of the differences between CPLD$_{ALL}$ and FIXDST$_{ALL}$, respectively.

[46] Table 5 summarizes the dust-induced changes in global and annual mean meteorological fields in FIXDST$_{ALL}$ and CPLD$_{ALL}$. Compared with the noninteractive experiment FIXDST$_{ALL}$, the stronger cooling in CPLD$_{ALL}$ leads to a larger reduction in humidity over the ocean. The global mean QAS decreases by 0.02 g kg^{-1} in CPLD$_{ALL}$. Additionally, the annual and global mean surface latent heat flux and sensible heat flux decrease by 0.77 W m^{-2} and 0.63 W m^{-2}, respectively. The magnitude of both changes is greater than that in FIXDST$_{ALL}$ so as to balance the larger cooling at the surface in CPLD$_{ALL}$. Precipitation shows stronger response in CPLD$_{ALL}$, which contributes to the increase of dust lifetime.

[47] Table 5 also lists global averages and the regional averages over the Saharan region from other four sensitivity experiments with either shortwave RF alone or longwave RF alone. Results in Table 5 show that the thermal effect of dust aerosol is non-negligible. No matter in the interactive (CPLD$_{SW/LW}$) or noninteractive (FIXDST$_{SW/LW}$) experiments, the thermal dust DRE mostly causes opposite climatic responses to that of the solar component. In some cases, the magnitude of the former is larger than the latter. Additionally, the climatic responses to the shortwave and longwave dust DRE are not additive. This explains why the responses to the net dust radiative effects shown in FIXDST$_{ALL}$ (CPLD$_{ALL}$) are not the sum of those in FIXDST$_{SW}$ (CPLD$_{SW}$) and FIXDST$_{LW}$ (CPLD$_{LW}$).

[48] The climatic responses to the dust aerosols are more regional than global (Table 5). The relatively short lifetime of dust particles limits their global transport. As a result, more dust mass is concentrated near source regions, leading to much larger climatic responses there [*Miller et al.*, 2004b].

6. Conclusions

[49] The equilibrium climate responses to the shortwave and/or longwave direct radiative forcings of dust are

Table 4. Simulated Dust Budget in Different Numerical Experiments[a]

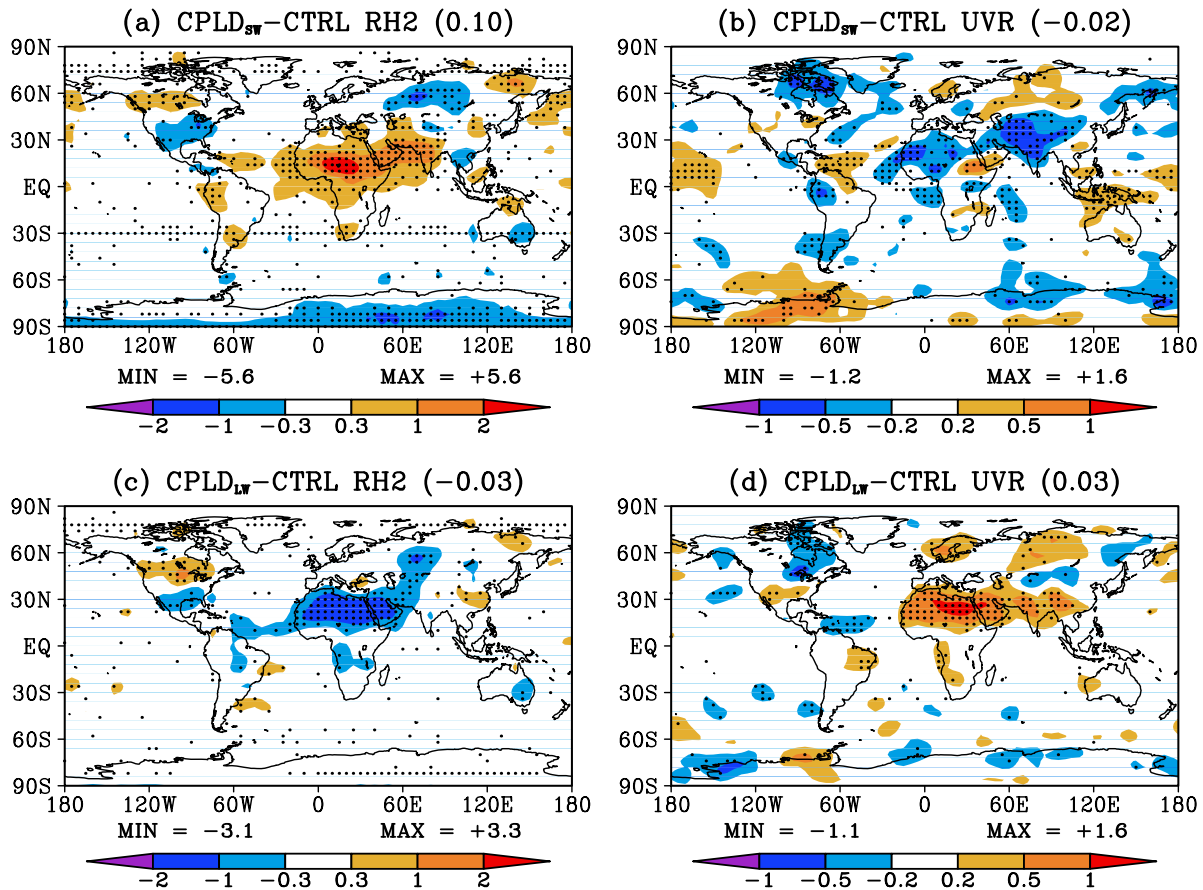| Experiments	Uplift (Tg yr^{-1})	Dry (Tg yr^{-1})	Wet (Tg yr^{-1})	Burden (Tg)	Lifetime (days)	DOT
CTRL	1900	1279	621	27.0	5.2	0.032
CPLD$_{SW}$	1797	1209	587	29.3	6.0	0.036
CPLD$_{LW}$	2009	1354	654	28.8	5.2	0.034
CPLD$_{ALL}$	1853	1248	605	30.5	6.0	0.037

[a]DOT, dust optical thickness.

Figure 11. Predicted annual mean changes relative to CTRL run in (a, c) surface air relative humidity and (b, d) friction velocity in (Figures 11a and 11b) CPLD$_{SW}$ and (Figures 11c and 11d) CPLD$_{LW}$. The differences that pass the 95% significance level are denoted with dots. The units of the relative humidity and friction velocity are % and cm s^{-1}, respectively.

examined in this work using the Global transport Model of Dust (GMOD) embedded within a general circulation model. In our control simulation without the feedback of dust radiative forcing into the GCM, the simulated dust uplift is 1900 Tg yr^{-1} for all four dust size bins ranging from 0.1 to 10 μm. Simulated global dust burden is 27.0 Tg and global mean DOT is 0.032 at 0.55 μm. On a global and annual mean basis, the estimated shortwave RF is -0.25 W m^{-2} at TOA and -1.95 W m^{-2} at the surface, while the longwave RF is $+0.27$ W m^{-2} at TOA and $+0.61$ W m^{-2} at the surface. Climatic effect of dust is simulated using two different approaches. In the first approach, monthly mean fields of dust simulated a priori are used in the radiative transfer module of the GCM to drive climate change, with levels of dust fixed during the climate integration (FIXDST simulations). In the second approach, dust aerosol interacts online with meteorology through dust cycle and its direct radiative effect (CPLD simulations).

[50] Dust shortwave RF is predicted to lead to a global and annual mean cooling that decreases with altitude, whereas dust longwave RF is predicted to lead to a global and annual mean warming that increases with altitude. These two effects counteract each other, leading to small changes in the annual and global mean air temperatures. With both longwave and shortwave RF of dust, predicted changes in global and annual mean surface air temperature and temperature at 200 hPa

are zero and $+0.12$ K, respectively, in FIXDST$_{ALL}$, and -0.06 K and $+0.05$ K in the CPLD$_{ALL}$ simulation. Despite of the small responses in global and annual mean temperature to the net RF of dust, it is important to consider both shortwave and longwave RF in climate simulations, because the shortwave effect dominates during the daytime and longwave effect alone exists at night. Predicted responses in surface air temperature show strong diurnal variation; over the Sahara Desert, as compared to the predicted annul mean change in surface air temperature of $+0.32$ K, the predicted changes in annual mean daytime (local 0900–1600) and nighttime (local 2100–0400) surface air temperature are -0.11 K and $+0.68$ K, respectively, in the FIXDST$_{ALL}$ simulation. On a global and annual mean basis, dust net RF leads to a reduction in precipitation by 0.02 mm d^{-1} in FIXDST$_{ALL}$ and by 0.03 mm d^{-1} in CPLD$_{ALL}$, with the reductions mainly a result of dust shortwave RF. Predicted changes in meteorological fields in all sensitivity simulations preformed in this work (Table 5) indicate that climate responses to shortwave and longwave RF of dust are nonlinear and are not additive.

[51] The feedback of dust-induced changes in meteorological fields into simulation of dust cycle indicates that dust shortwave and longwave RF play opposite roles in changing dust emissions. The solar DRE of dust increases surface humidity and reduces surface wind speed, leading to
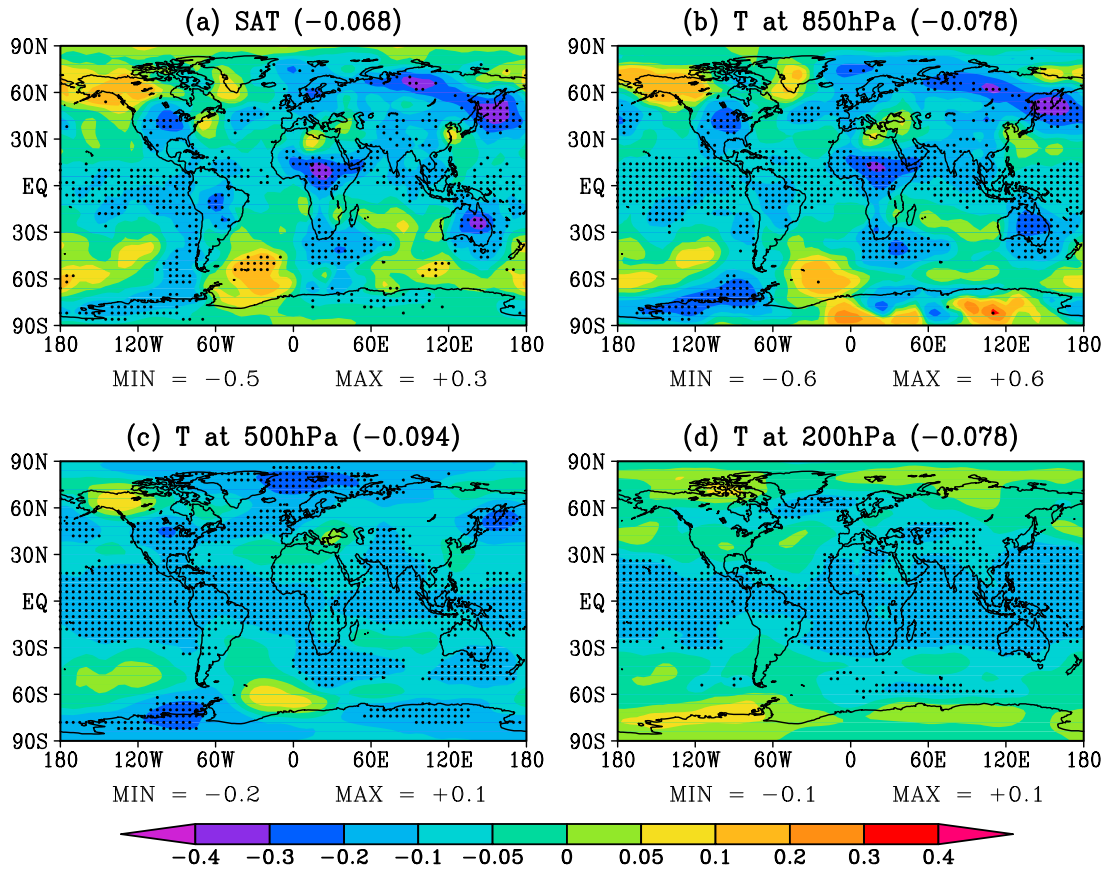
Figure 12. Differences in simulated annual mean air temperature at (a) surface, (b) 850 hPa, (c) 500 hPa, and (d) 200 hPa between CPLD$_{ALL}$ and FIXDST$_{ALL}$ (CPLD$_{ALL}$-FIXDST$_{ALL}$). Units: K.

reduction in dust uplift. On the contrary, the thermal RF increases dust mobilization through opposite effects. These results show that the thermal radiative effect of dust is non-negligible when quantifying its climatic influences.

[52] As compared with climate simulation with fixed monthly dust fields (FIXDST$_{ALL}$), dust-climate coupling in CPLD$_{ALL}$ leads to a 2% reduction in dust uplift as a result of the dust-induced increases in surface relative humidity and

Table 5. Simulated Annual Mean Changes in Meteorological Fields in Different Experiments[a]

	FIXDST$_{ALL}$	FIXDST$_{SW}$	FIXDST$_{LW}$	CPLD$_{ALL}$	CPLD$_{SW}$	CPLD$_{LW}$
			Global Mean			
SAT (K)	+0.00	−0.07	+0.15	−0.06	−0.14	+0.12
Air temperature at 850 hPa (K)	+0.02	−0.03	+0.15	−0.05	−0.11	+0.11
Air temperature at 500 hPa (K)	+0.07	−0.00	+0.20	−0.02	−0.11	+0.16
Air temperature at 200 hPa (K)	+0.12	+0.03	+0.22	+0.05	−0.06	+0.18
Surface air humidity (g kg^{-1})	+0.01	−0.02	+0.08	−0.02	−0.06	+0.06
Latent heat flux (W m^{-2})	−0.59	−0.76	+0.29	−0.77	−0.98	+0.29
Sensible heat flux (W m^{-2})	−0.52	−0.70	+0.17	−0.63	−0.72	+0.16
Precipitation (mm d^{-1})	−0.02	−0.03	+0.01	−0.03	−0.03	+0.01
Total cloud amount (%)	−0.08	−0.08	−0.03	−0.05	−0.10	−0.02
Middle cloud amount (%)	−0.13	−0.18	−0.02	−0.11	−0.19	+0.00
			Regional Mean Over Saharan Region[b]			
SAT (K)	+0.32	−0.50	+0.91	+0.23	−0.67	+0.90
Air temperature at 850 hPa (K)	+0.11	−0.04	+0.32	−0.02	−0.19	+0.27
Air temperature at 500 hPa (K)	+0.22	+0.13	+0.25	+0.16	+0.02	+0.21
Air temperature at 200 hPa (K)	+0.05	−0.03	+0.27	−0.06	−0.16	+0.20
Surface air humidity (g kg^{-1})	+0.12	+0.01	+0.11	0.14	−0.02	+0.08
Latent heat flux (W m^{-2})	+0.28	+0.15	+0.02	+0.50	+0.28	−0.06
Sensible heat flux (W m^{-2})	−7.57	−13.13	+5.79	−8.61	−13.4	+6.18
Precipitation (mm d^{-1})	+0.01	+0.00	−0.00	+0.02	+0.01	−0.00
Total cloud amount (%)	−0.11	−0.20	+0.05	−0.33	−0.67	−0.06
Middle cloud amount (%)	−0.54	−0.98	+0.02	−0.73	−1.31	−0.02

[a]All the changes are the differences between the specific experiment and the CTRL simulation.
[b]The Saharan region is [10°W to 30°E, 15–30°N]. SAT, surface air temperature.

wind speed. However, the reduction in precipitation by dust DRE increases dust burden by 13% (mostly the burden of small particles). In the meantime, the diurnal cycle of the dust transport in the interactive dust-climate simulation enhances the daytime cooling. As a result, more solar energy is scattered in CPLD$_{ALL}$ than in FIXDST$_{ALL}$, leading to a global mean stronger cooling of about 0.05 K from the surface to the higher troposphere in the coupled simulation.

[53] Note that this study examines the dust-climate coupling in the present-day atmosphere. The global climate responses to the RF of dust are found to be smaller than those to greenhouse gas forcing. Our subsequent study is to perform dust-climate coupled simulations for the paleoclimatic conditions, in which the dust loading shows an order of magnitude variation during glacial-interglacial cycles [*Mahowald et al.*, 2006; *Fischer et al.*, 2007; *Bar-Or et al.*, 2008].

References

Ackerman, S. A., and H. Chung (1992), Radiative effects of airborne dust on regional energy budgets at the top of the atmosphere, *J. Appl. Meteorol.*, *31*(2), 223–233, doi:10.1175/1520-0450(1992)031<0223:REOADO>2.0.CO;2.

Ahn, H. J., S. U. Park, and L. S. Chang (2007), Effect of direct radiative forcing of Asian dust on the meteorological fields in East Asia during an Asian dust event period, *J. Appl. Meteorol. Climatol.*, *46*(10), 1655–1681, doi:10.1175/JAM2551.1.

Alpert, P., Y. J. Kaufman, Y. Shay-El, D. Tanre, A. D. Silva, S. Schubert, and J. H. Joseph (1998), Quantification of dust-forced heating of the lower troposphere, *Nature*, *395*, 367–370, doi:10.1038/26456.

Bar-Or, R., C. Erlick, and H. Gildor (2008), The role of dust in glacial-interglacial cycles, *Quat. Sci. Rev.*, *27*(3–4), 201–208, doi:10.1016/j.quascirev.2007.10.015.

Batt, R. G., and S. A. Peabody (1999), Threshold friction velocities for large pebble gravel beds, *J. Geophys. Res.*, *104*(D20), 24,273–24,280, doi:10.1029/1999JD900484.

Briegleb, B. P. (1992), Delta-Eddington approximation for solar radiation in the NCAR Community Climate Model, *J. Geophys. Res.*, *97*(D7), 7603–7612.

Cakmur, R. V., R. L. Miller, J. Perlwitz, I. V. Geogdzhayev, P. Ginoux, D. Koch, K. E. Kohfeld, I. Tegen, and C. S. Zender (2006), Constraining the magnitude of the global dust cycle by minimizing the difference between a model and observations, *J. Geophys. Res.*, *111*, D06207, doi:10.1029/2005JD005791.

Carlson, T. N., and S. G. Benjamin (1980), Radiative heating rates for Saharan dust, *J. Atmos. Sci.*, *37*(1), 193–213, doi:10.1175/1520-0469(1980)037<0193:RHRFSD>2.0.CO;2.

Cautenet, G., M. Legrand, S. Cautenet, B. Bonnel, and G. Brogniez (1991), Thermal impact of Saharan dust over land. Part I: Simulation, *J. Appl. Meteorol.*, *31*, 166–180, doi:10.1175/1520-0450(1992)031<0166:TIOSDO>2.0.CO;2.

Christopher, S. A., and T. Jones (2007), Satellite-based assessment of cloud-free net radiative effect of dust aerosols over the Atlantic Ocean, *Geophys. Res. Lett.*, *34*, L02810, doi:10.1029/2006GL027783.

Claquin, T., M. Schulz, Y. Balkanski, and O. Boucher (1998), Uncertainties in assessing radiative forcing by mineral dust, *Tellus, Ser. B*, *50*, 491–505, doi:10.1034/j.1600-0889.1998.t01-2-00007.x.

de Rooij, W. A., and C. C. A. H. van der Stap (1984), Expansion of Mie scattering matrices in generalized spherical functions, *Astron. Astrophys.*, *131*, 237–248.

Fécan, F., B. Marticorena, and G. Bergametti (1999), Parametrization of the increase of the aeolian erosion threshold wind friction velocity due to soil moisture for arid and semi-arid areas, *Ann. Geophys.*, *17*, 149–157, doi:10.1007/s005850050744.

Fischer, H., M. L. Siggaard-Andersen, U. Ruth, R. Rothlisberger, and E. Wolff (2007), Glacial/interglacial changes in mineral dust and sea-salt records in polar ice cores: Sources, transport, and deposition, *Rev. Geophys.*, *45*(1), RG1002, doi:10.1029/2005RG000192.

Forster, P., et al. (2007), *Changes in atmospheric constituents and in radiative forcing, in Climate Change 2007: The Physical Science Basis. Contribution of Working Group I to the Fourth Assessment Report of the Intergovernmental Panel on Climate Change*, edited by S. Solomon et al., pp. 131–217, Cambridge Univ. Press, New York.

Ginoux, P., M. Chin, I. Tegen, J. M. Prospero, B. Holben, O. Dubovik, and S.-J. Lin (2001), Sources and distributions of dust aerosols simulated with the GOCART model, *J. Geophys. Res.*, *106*(D17), 20,255–20,273, doi:10.1029/2000JD000053.

Hansen, J., A. Lacis, D. Rind, G. Russell, P. Stone, I. Fung, R. Ruedy, and J. Lerner (1984), Climate sensitivity: Analysis of feedback mechanisms, in *Climate Processes and Climate Sensitivity, Geophys. Monogr. Ser.*, vol. 29, edited by J. E. Hanson and T. Takahashi, pp. 130–163, AGU, Washington, D. C.

Harrison, S. P., K. E. Kohfeld, C. Roelandt, and T. Claquin (2001), The role of dust in climate changes today, at the last glacial maximum and in the future, *Earth Sci. Rev.*, *54*(1–3), 43–80, doi:10.1016/S0012-8252(01)00041-1.

Haywood, J. M., R. P. Allan, I. Culverwell, T. Slingo, S. Milton, J. Edwards, and N. Clerbaux (2005), Can desert dust explain the outgoing longwave radiation anomaly over the Sahara during July 2003?, *J. Geophys. Res.*, *110*, D05105, doi:10.1029/2004JD005232.

Heinold, B., J. Helmert, O. Hellmuth, R. Wolke, A. Ansmann, B. Marticorena, B. Laurent, and I. Tegen (2007), Regional modeling of Saharan dust events using LM-MUSCAT: Model description and case studies, *J. Geophys. Res.*, *112*, D11204, doi:10.1029/2006JD007443.

Hu, M. C., and J. Z. Qu (1997), Preliminary estimate of dust deflation amount in Hexi Corridor, Gansu Province, in *Dust Storm Studies in China*, edited by Z. Y. Fang, pp. 118–120, Chinese Meteorol. Press, Beijing.

Iversen, J. D., and B. R. White (1982), Saltation threshold on Earth, Mars and Venus, *Sedimentology*, *29*, 111–119, doi:10.1111/j.1365-3091.1982.tb01713.x.

Jacobson, M. Z. (2001), Global direct radiative forcing due to multicomponent anthropogenic and natural aerosols, *J. Geophys. Res.*, *106*(D2), 1551–1568, doi:10.1029/2000JD900514.

Kalnay, E., et al. (1996), The NCEP/NCAR 40-Year Reanalysis Project, *Bull. Am. Meteorol. Soc.*, *77*(3), 437–471, doi:10.1175/1520-0477(1996)077<0437:TNYRP>2.0.CO;2.

Kaufman, Y. J., I. Koren, L. A. Remer, D. Rosenfeld, and Y. Rudich (2005), The effect of smoke, dust, and pollution aerosol on shallow cloud development over the Atlantic Ocean, *Proc. Natl. Acad. Sci. U. S. A.*, *102*(32), 11,207–11,212, doi:10.1073/pnas.0505191102.

Kim, M. K., W. K. M. Lau, M. Chin, K. M. Kim, Y. C. Sud, and G. K. Walker (2006), Atmospheric teleconnection over Eurasia induced by aerosol radiative forcing during boreal spring, *J. Clim.*, *19*(18), 4700–4718, doi:10.1175/JCLI3871.1.

Liang, X. (1996), Description of a nine-level grid point atmospheric general circulation model, *Adv. Atmos. Sci.*, *13*(3), 269–298, doi:10.1007/BF02656847.

Liao, H., and J. H. Seinfeld (1998), Radiative forcing by mineral dust aerosols: Sensitivity to key variables, *J. Geophys. Res.*, *103*(D24), 31,637–31,645, doi:10.1029/1998JD200036.

Liao, H., J. H. Seinfeld, P. J. Adams, and L. J. Mickley (2004), Global radiative forcing of coupled tropospheric ozone and aerosols in a unified general circulation model, *J. Geophys. Res.*, *109*, D16207, doi:10.1029/2003JD004456.

Liu, S. H., X. Yue, F. Hu, and H. Z. Liu (2004), Using a Modified Soil-Plant-Atmosphere Scheme (MSPAS) to simulate the interaction between land surface processes and atmospheric boundary layer in semi-arid regions, *Adv. Atmos. Sci.*, *21*(2), 245–259, doi:10.1007/BF02915711.

Lohmann, U., and K. Diehl (2006), Sensitivity studies of the importance of dust ice nuclei for the indirect aerosol effect on stratiform mixed-phase clouds, *J. Atmos. Sci.*, *63*(3), 968–982, doi:10.1175/JAS3662.1.

Lubin, D., S. K. Satheesh, G. McFarquar, and A. J. Heymsfield (2002), Longwave radiative forcing of Indian Ocean tropospheric aerosol, *J. Geophys. Res.*, *107*(D19), 8004, doi:10.1029/2001JD001183.

Lunt, D. J., and P. J. Valdes (2002), The modern dust cycle: Comparison of model results with observations and study of sensitivities, *J. Geophys. Res.*, *107*(D23), 4669, doi:10.1029/2002JD002316.

Luo, C., N. M. Mahowald, and J. D. Corral (2003), Sensitivity study of meteorological parameters on mineral aerosol mobilization, transport, and distribution, *J. Geophys. Res.*, *108*(D15), 4447, doi:10.1029/2003JD003483.

Mahowald, N. M., M. Yoshioka, W. D. Collins, A. J. Conley, D. W. Fillmore, and D. B. Coleman (2006), Climate response and radiative forcing from mineral aerosols during the last glacial maximum, pre-industrial, current and doubled-carbon dioxide climates, *Geophys. Res. Lett.*, *33*, L20705, doi:10.1029/2006GL026126.

Markowicz, K. M., P. J. Flatau, A. M. Vogelmann, P. K. Quinn, and E. J. Welton (2003), Clear-sky infrared aerosol radiative forcing at the surface and the top of the atmosphere, *Q. J. R. Meteorol. Soc.*, *129*(594), 2927–2947, doi:10.1256/qj.02.224.

Menon, S., J. Hansen, L. Nazarenko, and Y. F. Luo (2002), Climate effects of black carbon aerosols in China and India, *Science*, *297*(5590), 2250–2253, doi:10.1126/science.1075159.

Miller, R. L., and I. Tegen (1998), Climate response to soil dust aerosols, *J. Clim.*, *11*(12), 3247–3267, doi:10.1175/1520-0442(1998)011<3247: CRTSDA>2.0.CO;2.

Miller, R. L., J. Perlwitz, and I. Tegen (2004a), Feedback upon dust emission by dust radiative forcing through the planetary boundary layer, *J. Geophys. Res.*, *109*, D24209, doi:10.1029/2004JD004912.

Miller, R. L., I. Tegen, and J. Perlwitz (2004b), Surface radiative forcing by soil dust aerosols and the hydrologic cycle, *J. Geophys. Res.*, *109*, D04203, doi:10.1029/2003JD004085.

Mishchenko, M. I., J. M. Dlugach, E. G. Yanovitskij, and N. T. Zakharova (1999), Bidirectional reflectance of flat, optically thick particulate layers: An efficient radiative transfer solution and applications to snow and soil surfaces, *J. Quant. Spectrosc. Radiat. Transf.*, *63*, 409–432, doi:10.1016/ S0022-4073(99)00028-X.

Myhre, G., and F. Stordal (2001), Global sensitivity experiments of the radiative forcing due to mineral aerosols, *J. Geophys. Res.*, *106*(D16), 18,193–18,204, doi:10.1029/2000JD900536.

Overpeck, J., D. Rind, A. Lacis, and R. Healy (1996), Possible role of dust-induced regional warming in abrupt climate change during the last glacial period, *Nature*, *384*(6608), 447–449, doi:10.1038/384447a0.

Penner, J. E., et al. (2001), Aerosols: Their direct and indirect effects, in *Climate Change 2001: The Scientific Basis, Contribution of Working Group I to the Third Assessment Report of the Intergovernmental Panel on Climate Change*, edited by J. T. Houghton et al., pp. 291–336, Cambridge Univ. Press, New York.

Perez, C., S. Nickovic, G. Pejanovic, J. M. Baldasano, and E. Ozsoy (2006), Interactive dust-radiation modeling: A step to improve weather forecasts, *J. Geophys. Res.*, *111*, D16206, doi:10.1029/2005JD006717.

Perlwitz, J., I. Tegen, and R. L. Miller (2001), Interactive soil dust aerosol model in the GISS GCM: 1. Sensitivity of the soil dust cycle to radiative properties of soil dust aerosols, *J. Geophys. Res.*, *106*(D16), 18,167–18,192, doi:10.1029/2000JD900668.

Ramanathan, V., and P. Downey (1986), A nonisothermal emissivity and absorptivity formulation for water vapor, *J. Geophys. Res.*, *91*, 8649–8666, doi:10.1029/JD091iD08p08649.

Ramanathan, V., and M. V. Ramana (2005), Persistent, widespread, and strongly absorbing haze over the Himalayan foothills and the Indo-Gangetic Plains, *Pure Appl. Geophys.*, *162*(8–9), 1609–1626, doi:10.1007/s00024-005-2685-8.

Reddy, M. S., O. Boucher, Y. Balkanski, and M. Schulz (2005), Aerosol optical depths and direct radiative perturbations by species and source type, *Geophys. Res. Lett.*, *32*, L12803, doi:10.1029/2004GL021743.

Sassen, K. (2002), Indirect climate forcing over the western US from Asian dust storms, *Geophys. Res. Lett.*, *29*(10), 1465, doi:10.1029/ 2001GL014051.

Satheesh, S. K., C. B. S. Dutt, J. Srinivasan, and U. R. Rao (2007), Atmospheric warming due to dust absorption over Afro-Asian regions, *Geophys. Res. Lett.*, *34*(4), L04805, doi:10.1029/2006GL028623.

Shell, K. M., and R. C. J. Somerville (2007), Direct radiative effect of mineral dust and volcanic aerosols in a simple aerosol climate model, *J. Geophys. Res.*, *112*, D03206, doi:10.1029/2006JD007198.

Shi, G., H. Wang, B. Wang, W. Li, S. Gong, and T. Zhao (2005), Sensitivity experiments on the effects of optical properties of dust aerosols on their radiative forcing under clear sky condition, *J. Meteorol. Soc. Jpn.*, *83A*, 333–346, doi:10.2151/jmsj.83A.333.

Sokolik, I. N., and O. B. Toon (1996), Direct radiative forcing by anthropogenic airborne mineral aerosols, *Nature*, *381*(6584), 681–683, doi:10.1038/381681a0.

Sokolik, I. N., and O. B. Toon (1999), Incorporation of mineralogical composition into models of the radiative properties of mineral aerosol from UV to IR wavelengths, *J. Geophys. Res.*, *104*(D8), 9423–9444, doi:10.1029/1998JD200048.

Takemura, T., T. Nakajima, O. Dubovik, B. N. Holben, and S. Kinne (2002), Single-scattering albedo and radiative forcing of various aerosol species with a global three-dimensional model, *J. Clim.*, *15*(4), 333–352, doi:10.1175/1520-0442(2002)015<0333:SSAARF>2.0.CO;2.

Tanaka, T. Y., T. Aoki, H. Takahashi, K. Shibata, A. Uchiyama, and M. Mikami (2007), Study of the sensitivity of optical properties of mineral dust to the direct aerosol radiative perturbation using a global aerosol transport model, *SOLA*, *3*, 33–36, doi:10.2151/sola.2007-009.

Tegen, I., and I. Fung (1994), Modeling of mineral dust in the atmosphere: Sources, transport, and optical thickness, *J. Geophys. Res.*, *99*(D11), 22,897–22,914, doi:10.1029/94JD01928.

Tegen, I., and A. A. Lacis (1996), Modeling of particle size distribution and its influence on the radiative properties of mineral dust aerosol, *J. Geophys. Res.*, *101*(D14), 19,237–19,244, doi:10.1029/95JD03610.

Wang, Z., H. Ueda, and M. Huang (2000), A deflation module for use in modeling long-range transport of yellow sand over East Asia, *J. Geophys. Res.*, *105*(D22), 26,947–26,959, doi:10.1029/2000JD900370.

Washington, R., M. C. Todd, S. Engelstaedter, S. Mbainayel, and F. Mitchell (2006), Dust and the low-level circulation over the Bode'le' Depression, Chad: Observations from BoDEx 2005, *J. Geophys. Res.*, *111*, D03201, doi:10.1029/2005JD006502.

Weaver, C. J., P. Ginoux, N. C. Hsu, M.-D. Chou, and J. Joiner (2002), Radiative forcing of Saharan dust: GOCART model simulations compared with ERBE data, *J. Atmos. Sci.*, *59*(3), 736–747, doi:10.1175/ 1520-0469(2002)059<0736:RFOSDG>2.0.CO;2.

Woodward, S. (2001), Modeling the atmospheric life cycle and radiative impact of mineral dust in the Hadley Centre climate model, *J. Geophys. Res.*, *106*(D16), 18,155–18,166, doi:10.1029/2000JD900795.

Yoon, S. C., J. G. Won, A. H. Omar, S. W. Kim, and B. J. Sohn (2005), Estimation of the radiative forcing by key aerosol types in worldwide locations using a column model and AERONET data, *Atmos. Environ.*, *39*(35), 6620–6630, doi:10.1016/j.atmosenv.2005.07.058.

Yoshioka, M., N. M. Mahowald, A. J. Conley, W. D. Collins, D. W. Fillmore, C. S. Zender, and D. B. Coleman (2007), Impact of desert dust radiative forcing on Sahel precipitation: Relative importance of dust compared to sea surface temperature variations, vegetation changes, and greenhouse gas warming, *J. Clim.*, *20*(8), 1445–1467, doi:10.1175/JCLI4056.1.

Yue, X., and H. J. Wang (2009), The application of the CCM3/NCAR radiation scheme in IAP-AGCM, *Chin. J. Atmos. Sci.*, *33*(1), 16–28.

Yue, X., H. J. Wang, Z. F. Wang, and K. Fan (2009), Simulation of dust aerosol radiative feedback using the Global Transport Model of Dust: 1. Dust cycle and validation, *J. Geophys. Res.*, *114*, D10202, doi:10.1029/ 2008JD010995.

Zender, C. S., H. Bian, and D. Newman (2003), Mineral Dust Entrainment and Deposition (DEAD) model: Description and 1990s dust climatology, *J. Geophys. Res.*, *108*(D14), 4416, doi:10.1029/2002JD002775.

Zeng, Q., X. Zhang, X. Liang, C. Yuan, and S. F. Chen (1989), *Documentation of IAP Two-Level Atmospheric General Circulation Model*, DOE/ER/60314-H1, CDIAC TR044, 383 pp., Dept. of Energy, Washington, D. C.

Zhang, H. M., and M. F. Modest (2002), Evaluation of the Planck-mean absorption coefficients from HITRAN and HITEMP databases, *J. Quant. Spectrosc. Radiat. Transf.*, *73*(6), 649–653, doi:10.1016/S0022-4073 (01)00178-9.

Zhang, J., and S. A. Christopher (2003), Longwave radiative forcing of Saharan dust aerosols estimated from MODIS, MISR, and CERES observations on Terra, *Geophys. Res. Lett.*, *30*(23), 2188, doi:10.1029/ 2003GL018479.

Zhang, X. (1990), Dynamical framework of IAP nine-level atmospheric general circulation model, *Adv. Atmos. Sci.*, *7*(1), 67–77, doi:10.1007/ BF02919169.

————————————

K. Fan and H. Wang, Nansen-Zhu International Research Center, Institute of Atmospheric Physics, Chinese Academy of Sciences, PO Box 9804, Beijing 100029, China.

H. Liao, National Laboratory of Atmospheric Boundary Layer Physics and Atmospheric Chemistry, Institute of Atmospheric Physics, Chinese Academy of Sciences, Beijing 100029, China.

X. Yue, School of Engineering and Applied Sciences, Harvard University, 29 Oxford St., Cambridge, MA 02138, USA. (yuexu@mail.iap.ac.cn)